Highly crystalline sulfur-doped carbon nitride as photocatalyst for efficient visible-light hydrogen generation

Hao Wang[a], Yaru Bian[a], Jintang Hu[a], Liming Dai[a,b,*]

[a] BUCT-CWRU International Joint Laboratories, State Key Laboratory of Organic-Inorganic Composites, College of Energy, Beijing University of Chemical Technology (BUCT), Beijing, 100029, China
[b] Center of Advanced Science and Engineering for Carbon (Case4Carbon), Department of Macromolecular Science and Engineering, Case Western Reserve University (CWRU), 10900 Euclid Avenue, Cleveland, OH, 44106, USA

ARTICLE INFO

ABSTRACT

Heteroatom-doping is an efficient approach to extend optical absorption beyond 460 nm, which, however, often reduces crystallinity to cause a concomitant detrimental effect on photocatalytic activity. In the present study, we developed a facile approach to synthesize S-doped g-C$_3$N$_4$ with a high crystallinity by self-assembling melamine and tri-thiocyanuric acid, followed by calcination. The resultant optimal S-doped carbon nitride (MTCN-6) exhibited a super-high H$_2$-generation rate of 1511.2 µmol g^{-1} h^{-1} (about 11 times higher than that of the pristine CN) under visible light excitation ($\lambda > 420$ nm) and an excellent AQE of 3.9% at 420 nm.

1. Introduction

Having a high energy density close to that of gasoline [1,2], hydrogen is one of the ideal ecofriendly energy storage chemicals with water as the only combustion product. Thus, low-cost and efficient generation of hydrogen fuel has attracted a great deal of interest. Among various methods developed for hydrogen production [3], the solar-driven generation of hydrogen from water is the most attractive option as water and sunlight are both renewable and earth abundant [4]. However, effective semiconductor photocatalysts are required for hydrogen generation from photocatalytic water splitting. In this regard, graphitic carbon nitrides have been regarded as very promising candidates due to their easy preparation, low cost, nontoxicity, good chemical and thermal stability, and suitable band gap for solar water splitting [5–7]. However, efficient solar water splitting is still limited because of the low electrical conductivity, high recombination rate of photo-carriers, and narrow absorption range of visible light intrinsically associated with the pristine g-C$_3$N$_4$ (CN) [5,8]. To address these drawbacks, various innovative approaches, including morphology control [9], crystallinity improvement [10], modulation of electronic structure *via* heteroatom doping [11], deposition of co-catalysts [12], and creation of hetero-junctions with other semiconductors [13–15], have been recently reported [16]. Among them, doping heteroatom into the lattice of CN is an effective way to extend the light absorption tail beyond 460 nm (the absorption edge of the pristine CN), which is critical for CN photocatalyst to be used for solar water splitting.

Furthermore, heteroatom sites can also serve as trapping sites for electrons or cavities to suppress the recombination.

Of particular interest, an I-doped carbon nitride was demonstrated to show an absorption region from 420 to 600 nm, exhibiting an optimum hydrogen generation rate of ~ 38 µmol h^{-1} with an apparent quantum efficiency of 2.4% at 420 nm [17]. However, heteroatom-doping often causes the degradation of crystallinity whereas a high crystallinity (or low structural imperfection) is necessary for efficient charge transfer to ensure high photocatalytic performance [10,11,18,19]. Thus, it is important to widen the optical absorption region with a minor or no decrease in crystallinity by minimizing the trade-off effects of the heteroatoms doping, through controlling synthesis of heteroatom-doped CNs with an optimized dopant content.

Herein, we report a facile approach to synthesize S-doped CN *via* self-assembling of melamine with tri-thiocyanuric acid, followed by calcination (Scheme 1). The resultant S-doped CN contains a small amount of sulfur dopant (0.14 wt. %,), but sufficient to extend the optical absorption, and displays a high crystallinity (even higher than that of the pristine CN), presumably due to the retaining of the well-ordered structure in the high-melting-point melamine-tri-thiocyanuric acid supramolecular precursor even during and after calcination. It was found that the optimized S-doped CN (designated as MTCN-6) exhibited an approximately 11 times higher hydrogen generation rate than that of the pristine CN under visible light excitation ($\lambda > 420$ nm) with a very high apparent quantum efficiency (AQE) 3.90% at 420 nm. This work represents an important advancement in rational design and synthesis
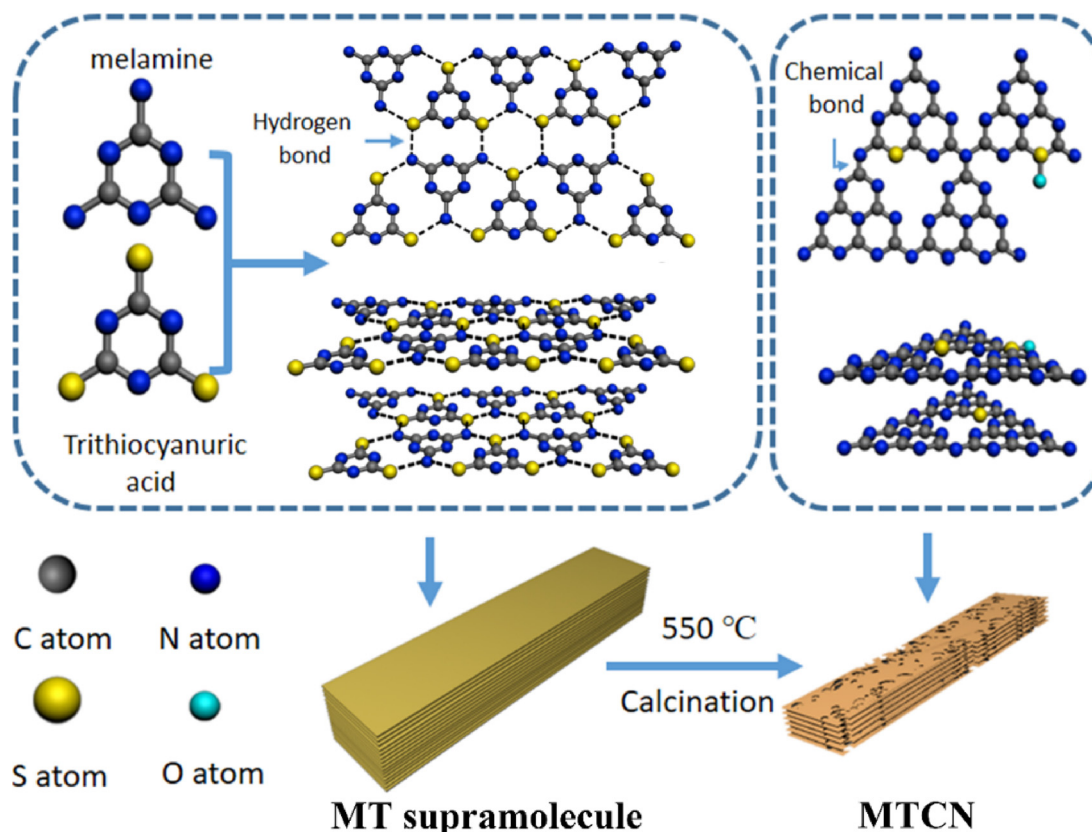

Scheme 1. Schematic representation of the synthesized process of MTCN.

of heteroatom-doped CNs with high photocatalytic performance for cost-effective mass production of hydrogen gas, and hence hydrogen energy.

2. Experimental section

Melamine (1.000 g, 8 mmol) and tri-thiocyanuric acid (1.410 g, 8 mmol) were purchased from Macklin (Shanghai, China) and used without further purification. They were dissolved into 50.0 mL distilled water (DI water) and 25.0 mL *N, N*-dimethyl formamide (DMF, A.R., Beijing Chemical works, China) at 80 °C, respectively, to obtain homogeneous solutions. After stirring (1500 W, 200 rmp, ETS-D5, IKA, Germany) for 0.5 h, the resultant aqueous solution of melamine was dropwisely added into tri-thiocyanuric acid solution to obtain a light yellow mixture, which was further stirred for 0.5, 3, 6, and 12 h at 80 °C to generate intermediate products designated as MT-X (X stands for the stirring and heating time). Upon cooling down to room temperature (20 °C), 250 mL DI water was added into the mixture solution, which was further stirred for 12 h under the ambient condition. By vacuum filtering, light yellow supramolecular MT-X samples were obtained and dried in oven at 60 °C for 12 h, which were then annealed in a tubular furnace heated up to 550 °C at a heating rate of 5 °C min^{-1} in air for 4 h to produce the final products MTCN-X (X stands for the stirring time). For comparison, the pristine CN was synthesized by direct annealing melamine (5 g) in a tubular furnace under the same conditions for MTCN-X.

3. Physicochemical characterization

X-ray powder diffraction (XRD) was measured on a D2 PHSDER X-ray diffractometer (Bruker Company, Germany) using Cu Kα radiation (γ = 1.54056 Å). Fourier transform infrared (FT-IR) spectroscopic measurements were carried out using KBr pellets on a Nicolet 6700 FT-

IR spectrometer (Thermo scientific, USA) with DLA TGS detector. X-ray photoelectron spectroscopy (XPS) was performed on an ESCALAB MKII X-ray photoelectron spectrometer (VG Instruments, CA, USA) using non-monochromatized Mg–Kα X-ray source. Elemental analysis (EA) was done on a vario EL cube (Elementer, Germany). UV–vis diffuse reflectance spectra (DRS) were taken on a UV-2600 spectrophotometer (Shimadzu, Japan). Photoluminescence (PL) spectroscopy was performed using an F-700 fluorescence spectrophotometer (Hitachi, Japan) with 368-nm excitation laser. Time-resolved fluorescence spectrosocpy was monitored on an FLS980 spectrophotometer (Edinburgh, England) with exciton wavelength at 370 nm. Transmission electron microscope (TEM) images were acquired on a FEI Tecnai G20 field emission electron microscope operating at an accelerating voltage of 200 kV. N$_2$ absorption and desorption isotherms were collected on an ASAP 2460 N$_2$ absorption apparatus (Micrometritica, USA) at 77 and 273 K, respectively. The total pore volume was estimated from the adsorbed amount of N$_2$ at a relative pressure of P/P$_0$ = 0.995.

4. Electrochemical measurements

Electrochemical impedance spectroscopy (EIS) was performed on an electrochemical workstation (CHI 760E) with a standard three-electrode cell containing saturated KCl as the electrolyte by using an indium-tin oxide glass (FTO glass) pre-coated with the carbon nitride samples as the working electrode, Pt wire and Ag/AgCl as counter and reference electrode, respectively. The working electrode was prepared by drop coating. More specifically, we first prepared the ink by dispersing 20.000 mg specific carbon nitride powder in a mixture solution of 1.0 mL ethanol, 1.0 mL ethylene glycol, and 20.0 μL Nafion (5*wt.*%), followed by 0.5 h sonication. Then, we drop-cast 400.0 μL of the resulted colloidal dispersion onto a piece of FTO glass (2 × 1.5 cm^2) with an effective area of 1.5 cm^2 for the sample coverage. Prior to use, the resultant electrode was dried in an oven at 120 °C for 12 h to enhance a

good adhesion between the sample and electrode.

5. Photocatalytic performance measurements

Photocatalytic performance for H_2 generation was investigated in a 300 mL pyrex flask under a 300 W Xe lamp (Microsolar 300, Perfect Light) with a cut filter ($\lambda > 420$ nm) as the light source. Typically, 40.0 mg of a specific carbon nitride (CN) sample was added to an aqueous solution (80.0 mL) of triethanolamine (TEOA, 20 vol. %, as a sacrificial reagent). Then, ca.1.0 wt. % Pt was deposited onto the surface of CN by *in situ* photo-deposition approach using $H_2PtCl_6\cdot6H_2O$ as Pt source under 300 W Xe lamp, irradiating for 1 h without cut filter. Pt was used as co-catalyst to facilitate charge separation and reduce the overpotential of hydrogen evolution reaction (HER). The resulting suspension was then bubbled with N_2 at flow of 200 sccm for 0.5 h to remove dissolved oxygen. After irradiation under visible light (300 W Xe lamp with a $\lambda > 420$ nm cut filter) for 3 h, 0.5 mL of the released gas was sampled by using gas chromatograph (TCD with N_2 as a carrier gas and 5 Å molecular sieve column, GC-2014C, SHIMADZU) to test the amount of H_2 generated. The stability of photocatalyst was measured using the same protocol with a prolonged sampling duration. For recycling the photocatalyst, we collected the photocatalyst residue by centrifuging the reaction solution, washed the photocatalyst residue for several times with DI water, and dried the purified photocatalyst residue in an oven (DGX-9053B-1, Shanghai Fuma Test Equipment Co. Ltd, Shanghai, China) at 80℃. The apparent quantum efficiency (AQE) was measured under the same reaction condition with a band-pass filter ($\lambda = 420$ nm) and an irradiation time of 24 h with an average irradiation intensity of 8.8 mW cm^{-2}. The irradiated cross-sectional area was 6.3 cm^2. The AQE value was calculated according to Eq. (1) [11]:

$$AQE = \frac{number\ of\ evolved\ hydrogen\ molecules \times 2}{number\ of\ incident\ photons} \times 100\% \tag{1}$$

6. Results and discussion

Scheme 1 shows the reaction route to MTCN with the detailed synthetic procedures given in the Experimental section. Briefly, melamine (1.000 g) and tri-thiocyanuric acid (1.410 g) were dissolved in DI water (50.0 ml) and DMF (25.0 ml), respectively, at 80 °C under stirring for 0.5 h. Thereafter, the aqueous solution of melamine was added dropwisely into the tri-thiocyanuric acid solution in DMF, and further stirred for 0.5, 3, 6, and 12 h at 80 °C to form rectangular rod-like supramolecular assemblies, MT-X (X = 0.5, 3, 6, 12) *via* the hydrogen bond formation between $-NH_2$ of melamine and $-S$ of tri-thiocyanuric acid. Subsequent calcination of MT-X (X = 0.5, 3, 6, 12) led to MTCN-X (X = 0.5, 3, 6, 12). The S atoms in tri-thiocyanuric acid acted as dopants for the in-situ S-doping with a concomitant release of H_2S, as reflected by a serious egg smell from the quartz tube furnace after calcination.

To verify the formation of MT supramolecular assembly, we recorded XRD patterns of melamine, tri-thiocyanuric acid, and MT-6 (Fig. S1). As can be seen, MT-6 shows a crystal structure different from that of either melamine or tri-thiocyanuric acid. For a MT-6 crystal, the XRD peaks at 11.6° and 21.2° can be assigned to the (100) and (200) of in-plane stacking, respectively, while the peak centered at 29.8° is attributable to a (002) (0.299 nm) crystal face corresponding to the graphite-like packing of a layered structure [20]. As can be seen in Fig. S2 (*cf.* Scheme 1), the hydrogen-bonding-induced 2D assemblies might have stacked together to form a rectangular rod-like MT-6 crystal with a width of 3–20 μm and a length of 20–50 μm.

Fig. 1a reproduces a SEM image of MTCN-6, which, together with Fig. S2b&c, shows a rectangular shape similar to that of MT-6 (Fig. S2a). The corresponding TEM images in Figs. 1b&S3c shows some wrinkled meso/macropores, presumably caused by the release of H_2S gas during calcination. Unlike MT-6 or MTCN-6, CN shows no regular

shape (Figs. S2d and S3a&b). SEM images of MTCN-0.5 and MTCN-3 given in Fig. S4a and b shows many irregularly-shaped particles mixed with nano-macro rods, whereas the corresponding SEM images of MTCN-6 and MTCN-12 given in Fig. S4c and d shows the disappearance of those irregularly-shaped particles with slightly enlarged nano-macro rods, which could be attributed to the Ostwald ripening effect [21].

Fig. 1c shows XRD profiles for MTCN-6 and CN, both of which exhibit two pronounced peaks at 13.1° and 27.1° attributable to (100) and (002) crystal face characteristic of graphitic-like carbon nitride crystal structure [22]. Although MTCN-6 has same crystal structure as that of CN, its (002) peak intensity is more narrower and shifts to a slightly higher angle than that of CN, corresponding to a decrease in the lattice distance from 0.328 nm for CN [10] to 0.325 nm for MTCN-6. The decrease in the c-axis direction indicates strong interactions between the π-π stacked large aromatic supramolecular layers in MTCN-6, which should also facilitate the interlayer charge transfer. Compared to CN, the small, but noticeable, decrease in the (002) half-peak width and increase in the peak intensity, relative to the (001) peak intensity, indicating the presence of a relatively large crystal domain with less defects in the MTCN-6 crystal framework [23], which is consistent with the element analysis data that shows the C/N molar ratio increased from 64.83% for CN to 66.42% for MTCN-6. Crystal lattice shown in the inset of Fig. 2b provides additional evidence for high crystallinity of MTCN-6 [24]. XRD patterns for MTCN-X (X = 0.5, 3, 6, 12) show that the (002) peak intensity and shift increased initially with increasing in the stirring time from 0.5 to 6 h, and then leveled off with further increasing in the stirring time (Fig. S5).

Fig. 1e shows FTIR spectra of MTCN-6 and CN. As can be seen, the wide IR band over 1200–1650 cm^{-1} is typical skeletal stretching vibrations of C-N heterocycle [25]. The IR peak at 807 cm^{-1} is characteristic of the breathing mode of heptazine rings indicates the presence of the heptazine ring building blocks. The other broad band over 2900–3300 cm^{-1} is arising from the N-Hx (x = 1 or 2) stretching vibrations, and the adsorption peak centered at 3430 cm^{-1} could be attributed to the stretching vibrations of adsorbed water molecules [26]. These results indicate the formation of the 2D supramolecular assemblies, as shown in Scheme 1.

To measure the specific surface area and porosity, we performed N_2 adsorption and desorption measurements. As shown in Fig. 1f, the BET isotherms for both CN and MTCN-6 can be attributed to type IV with type H_3 loops, indicating the presence of mesopores (23 nm, inset of Fig. 1f). The calculated specific surface area (SSA) and pore volume increased from 16.3 m^2 g^{-1} and 0.06 cm^3 g^{-1} for CN to 66.4 m^2 g^{-1} and 0.39 cm^3 g^{-1} for MTCN-6, respectively. The overall more than four times increase in the specific surface area and pore volume for MTCN-6 over CN could significantly increase its (photo)catalytic activity, as we shall see later.

As expected, EDS element mapping for MTCN-6 (Fig. S6) shows the presence of homogeneously-distributed C, N, O, and S elements. Further chemical information for the MTCN-6 and CN was obtained from X-ray photoelectron spectroscopic (XPS) measurements. As can be seen from Fig. S7a&b, the XPS survey spectra of both MTCN-6 and CN show the presence of C, N, and O elements, with a small amount of S for the former. Fig. 2a shows the high-resolution XPS C1s spectrum of MTCM-6, which can be deconvoluted into four component peaks attributable to the *sp2*-hybridized C atoms in the heptazine ring (N−C═N, 287.9 eV) [27], C═C/C−C (284.8 eV) [28] from adventitious carbon (carbon conductive tapes), C−S−C (284.0 eV) [29], C−O (286.3 eV) and C−N Hx (x = 1 or 2) (288.8 eV) [11], respectively. The presence of XPS C1s peak components for the heptazine ring indicates the fundamental framework of graphite-like carbon nitride is preserved in MTCN-6. Fig. 2b shows the high-resolution XPS N1s spectrum deconvoluted into the *sp2*-hybridized N in the N-containing aromatic ring (C−N═C, 398.3 eV), tertiary N in N−(C)$_3$ moieties (399.6 eV), and N in C−N−H (x = 1 or 2) (400.7 eV) [30]. The weak broad band centered at 404.0 eV is most likely arising from charging effects [30] associated with S-doping of the
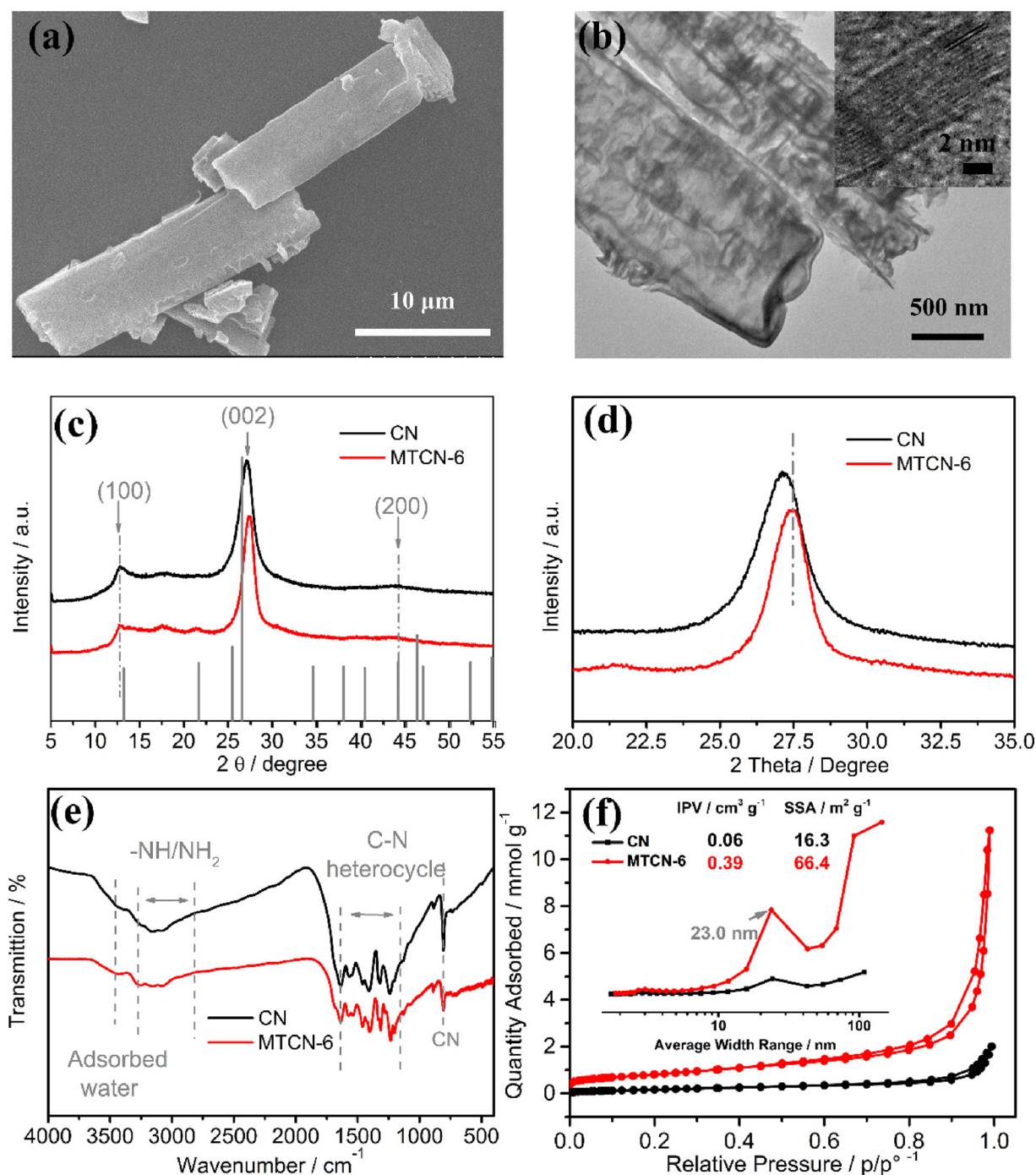
Fig. 1. (a) SEM, and (b) TEM image of MTCN-6. Inset: High-magnification TEM image. (c, d) XRD patterns, (e) FT-IR spectra, (f) N_2 adsorption and desorption isotherms, insert showing the corresponding pore size distributions for CN and MTCN-6.

conjugated supramolecular assemblies.

Fig. 2c reproduces the high-resolution XPS S2p spectrum, which shows a peak at 168.0 eV attributable to sulfur oxide (S−O) formed during calcination, while another peak at 163.7 eV arising from the S-doping by replacing N atoms in some heptazine rings with S atoms to form the C−S−C bonds [19], which was consisted with the result of S2p. Therefore, the presence of O peaks in Fig. S7a&b indicates the formation of −C−O /−S−O, though the presence of some physically absorbed O_2 molecules cannot be ruled out [31]. Compared with the high-resolution XPS C1 s and N1 s peaks of CN (Fig. S7c&d), the corresponding peaks for MTCN-6 (Fig. 2a&b) shifted slightly towards higher binding energies, indicating the S-doping induced changes in the

surface electronic structure. The presence of S in MTCN-6 is further confirmed by elemental analysis (Table S1). The valence band energy level was calculated from Fig. 2d, which is 1.69 eV for CN and 1.48 eV for MTCN-6 (see, SI for detailed calculations of VB).

Along with the S-doping induced electronic modulation, the optical properties of MTCN-6 could also be altered. As expected, Fig. 3a shows the appearance of an obvious absorption tail over 450–700 nm for MTCN-6 compared with CN, indicating the important effects of S-doping on the band gap (Eg) [32]. After the K-M-plot transform [11], the obtained Eg value decreased from 2.71 eV for CN to 2.64 eV for MTCN-6. Compared to CN, Figure S8 shows different shape in the optical absorption and band gap for others MTCN-X (X = 0.5, 3, 12). With
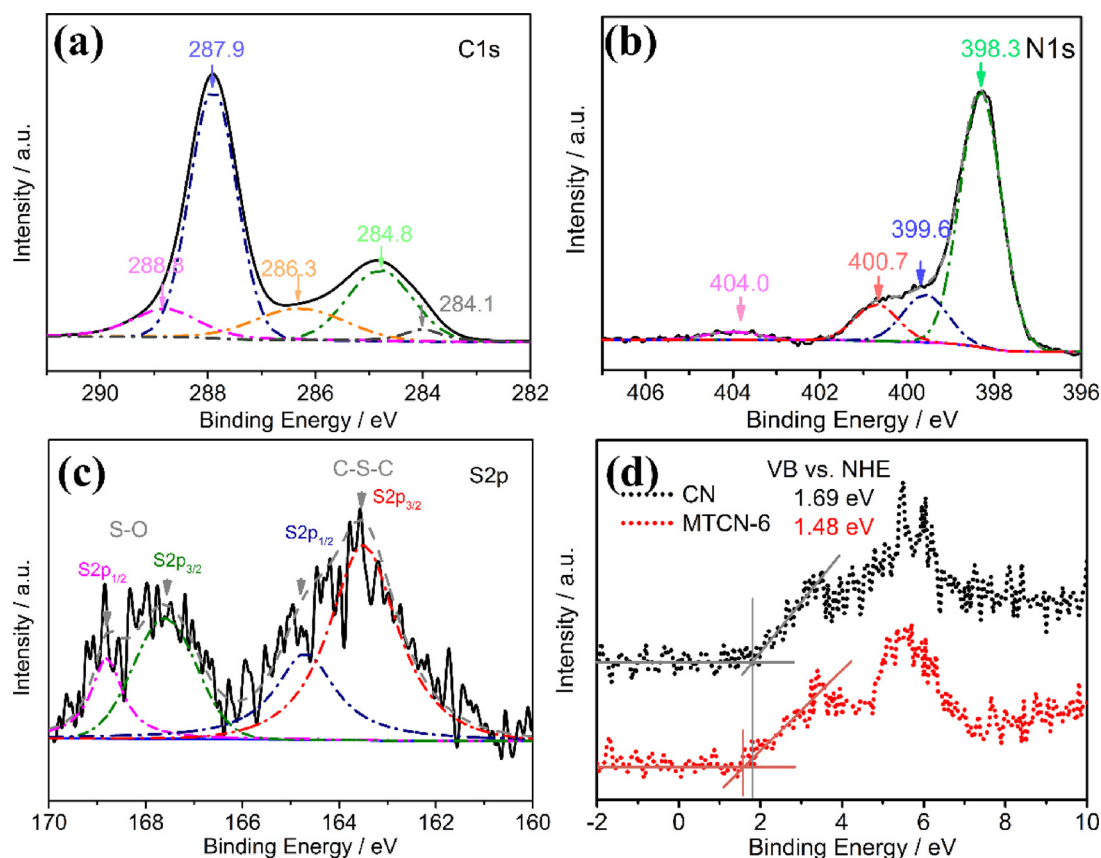
Fig. 2. XPS high-resolution spectra of (a) C 1 s, (b) N 1 s, and (c) S2p of MTCN-6; (d) XPS VB spectra of CN and MTCN-6.
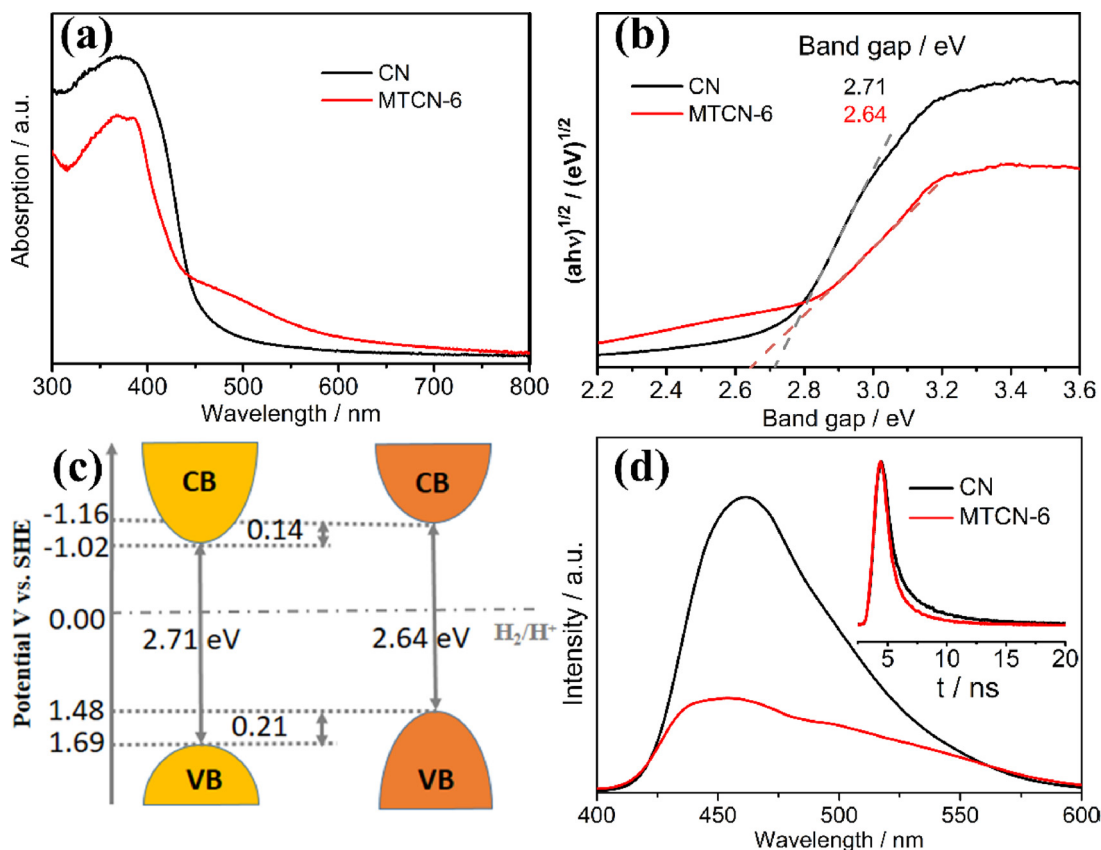

Fig. 3. (a) UV–vis diffuse reflectance spectra (DRS), (b) K-M-plot, (c) electronic band gap structure of CN (*Left*) and MTCN-6 (*Right*), and (d) PL spectra of CN and MTCN-6. Inset shows the time-resolved fluorescence kinetics monitored at the excitation wavelength of 373 nm.
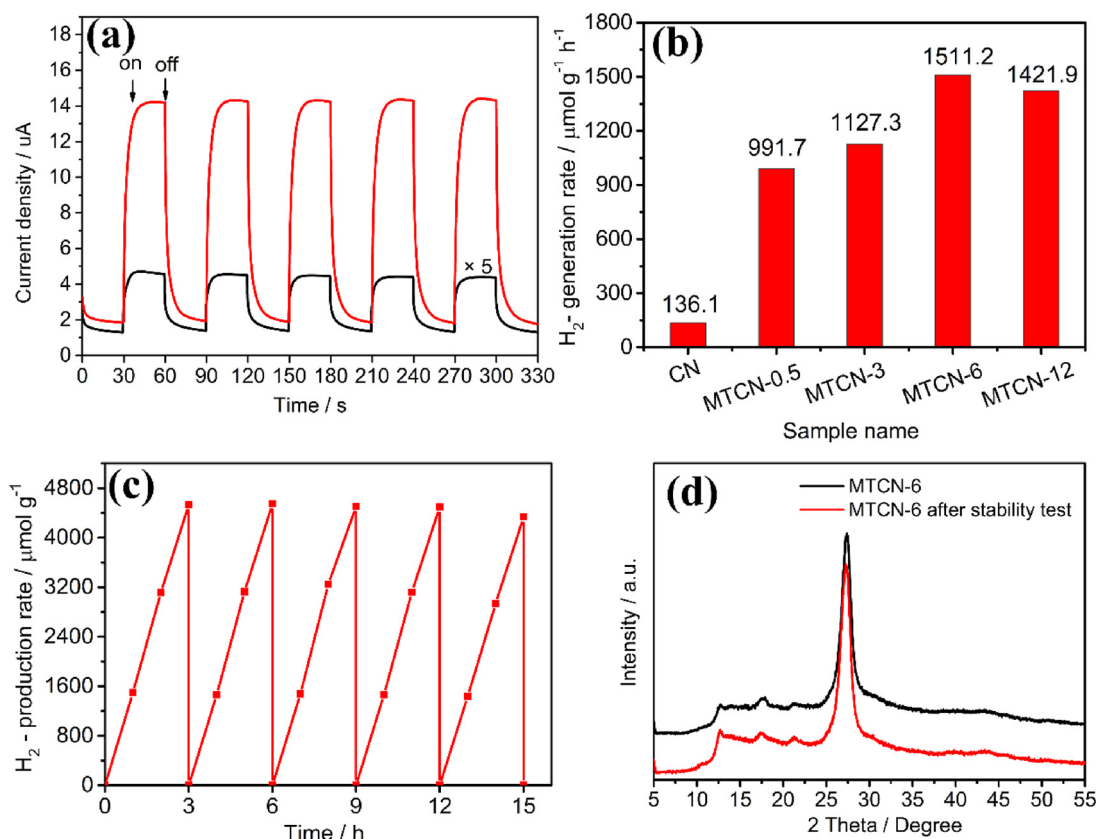
Fig. 4. (a) Photocurrent of MTCN-6 and CN (the photocurrent of CN was multiplied by 5 for clarity), (b) H_2-generation rate of CN and MTCN-X (X = 0.5, 3, 6, 12), (c) stability test of MTCN-6, and XRD pattern of MTCN-6 and MTCN-6 after the stability testing.

the increasing of stirring time, the value band gap shows decreasing trend form 2.84 eV for MTCN-0.5 to 2.63 eV for MTCN-12, which can be explained by the difference in crystallinity of products.

Apart from a proper Eg, energy level matching between the conduction band (CB) position of a photocatalyst and the reduction potential of proton is also an important parameter to determine whether or not the water splitting reaction can occur [33]. Combination of the VB energies deduced from Fig. 2d with the band gap (Eg) values derived from K-M-plots (Fig. 3b) [34] allowed us to determine the energy levels of CB and VB for MTCN-6 and CN [3,35]. As can be seen in Fig. 3c, the CB values for MTCN-6 and CN are both below the reduction potential of proton (0 eV), indicating that electrons photo-excited into CB can meet the thermodynamic requirement for reducing H^+ to H_2 under irradiation at appropriate wavelength of visible light [8]. Furthermore, the CB position of MTCN-6 is more negative than that of CN, and hence has a higher capability for reducing protons to generate hydrogen gas.

Photoluminescence (PL) was used to measure the efficiency of charge carrier separation, transfer, and trapping. Fig. 3d shows the PL emission spectra of CN and MTCN-6. Compared to CN, MTCN-6 exhibited a dramatic decrease in the PL peak intensity, indicating an effective inhibition of the carrier-recombination in MTCN-6 [17]. This is because minor S dopants can behave as trapping sites to avoid the recombination of charge carries [32] and high crystallinity can suppress electron-hole recombination by enhancing the charge mobility in MTCN-6 [10]. To confirm that MTCN-6 has a good carrier separation ability, radiative lifetimes of the recombining photo-carriers (Fig. 3d, inset) were monitored by time-resolved fluorescence (Table S2) [15]. Table S2 shows an average excitation lifetime (τ_A) of 1.29 ns for MTCN-6, which is notably shorter than that of CN (3.28 ns). The reduced τ_A for MTCN-6 implies an enhanced excitation dissociation, indicating effective separation of photo-induced carriers [24]. EIS spectra reflect the charge transfer rate, and hence the reaction rate, on the surface of the

electrode [36,37]. As can be seen in Figure S9, MTCN-6 shows the smallest radius of the arc, suggesting the most effective charge separation and interfacial charge transfer rates for photo-induced carriers among all the samples investigated in this study. Although MTCN-6 shows a similar XRD (002) peak intensity as that of MTCN-12 (Figure S5), it exhibited a smaller PL emission peak due to a faster interfacial charge transfer (Figure S10), and hence less charge recombination, associated with a small crystal size, namely, short carrier transfer distance (Figure S4c and d). These results indicate that MTCN-6 would be the best catalyst for photocatalytic hydrogen generation.

To investigate the photocatalytic performance of MTCN-6 and CN for hydrogen generation, we performed photocurrent density measurements [38]. As expected, MTCN-6 showed a noticeable current increase upon visible light irradiation (λ > 420 nm), followed by a quick reverse back to the original state upon removal of the light source (Fig. 4a). The almost constant current intensity observed during different cycles under the light irradiation indicates a stable photocatalytic performance of MTCN-6. The observed dramatic enhancement in the photocurrent response for MTCN-6, together with its relatively low PL intensity and smaller arc radius of EIS impedance than that of CN, confirming that the MTCN-6 has an effectively enhanced charge transfer capability and reduced charge recombination.

We further investigated the photocatalytic performance of CN and MTCN-X (X = 0.5, 3, 6 and 12) for hydrogen generation from the photocatalytic water splitting by using 1 wt. % Pt as co-catalyst and 20 vol. % TEOA as sacrificial reagent. Fig. 4b shows a low hydrogen generation rate (136.1 μmol g^{-1} h^{-1}) for the pristine CN due to its low crystallinity, limited optical adsorption, small specific surface area/pore volume, poor charge generation and transfer rate, and relatively low photo-induced reducibility (cf. Fig. 3c). The H_2 generation rate for MTCN-0.5 is about 7.3 times higher than that of CN caused by S-doping. H_2-generation rate increased from 991.7 μmol g^{-1} h^{-1} for MTCN-0.5

to 1511.2 μmol g^{-1} h^{-1} for MTCN-6, suggesting crystallinity has important effects on improving photocatalytic activity apart from the S-doping. Compared to MTCN-6, however, MTCN-12 exhibited a decreased H$_2$ generation rate of 1421.9 μmol g^{-1} h^{-1} from 1511.2 μmol g^{-1} h^{-1} for MTCN-6 in accordance with PL spectra (Fig. 3d). Fig. 4c displays a typical stability test for MTCN-6 over 5 cycles, which shows no obvious decrease in the H$_2$ generation rate. After the 15 h stability testing, we also performed XRD measurement for the used MTCN-6 and no obvious difference was found before and after the stability test. These results indicate that MTCN-6 has an excellent photocatalytic stability. Furthermore, MTCN-6 shows the highest photocatalytic activity among MTCN-X (X = 0.5, 3, 6, 12) with a pretty high AQE efficiency of 3.9% under 420 nm irradiation calculated from Eq. (1).

7. Conclusions

In summary, we have successfully synthesized a highly crystalline S-doped carbon nitride (MTCN-6) with rectangular rod-like morphology by self-assembling melamine and tri-thiocyanuric acid, followed by calcination. Compared to the pristine carbon nitride (CN), the resultant S-doped 2D supramolecular assembly (MTCN-6) possesses a significantly increased specific surface area, enhanced visible light adsorption, and optimal electronic and band gap structure for photocatalytic hydrogen generation. Consequently, the newly-development MTCN-6 shows a super-high H$_2$-generation rate of 1511.2 μmol g^{-1} h^{-1}, which is about 11 times higher than that of the pristine CN, under visible light excitation (λ > 420 nm) and an excellent of AQE 3.9%.

Acknowledgments

Appendix A. Supplementary data

Supplementary material related to this article can be found, in the online version, at doi:https://doi.org/10.1016/j.apcatb.2018.07.023.

References

[1] C. Hu, L. Dai, Adv. Mater. 29 (2017).
[2] J. Zhang, L. Qu, G. Shi, J. Liu, J. Chen, L. Dai, Angew. Chem. Int. Ed. 128 (2016) 2270–2274.
[3] Z. Hong, B. Shen, Y. Chen, B. Lin, B. Gao, J. Mater. Chem. A 1 (2013) 11754.
[4] X. Wang, J.M. Carlsson, K. Domen, K. Maeda, A. Thomas, T. Kazuhiro, Nat. Mater. 8 (2009) 76–80.
[5] W. Ong, L. Tan, Y. Ng, S. Yong, S. Chai, Chem. Rev. 116 (2016) 7159–7329.
[6] Q. Han, B. Wang, J. Gao, Z. Cheng, Y. Zhao, Z. Zhang, L. Qu, ACS Nano 10 (2016) 2745–2751.
[7] B.W. Qing Han, Yang Zhao, Chuangang Hu, Liangti Qu, Angew. Chem. Int. Ed. Engl. 54 (2015) 11433–11437.
[8] J. Liu, H. Wang, M. Antonietti, Chem. Soc. Rev. 45 (2016) 2308–2326.
[9] P. Niu, L. Zhang, G. Liu, H.-M. Cheng, Adv. Funct. Mater. 22 (2012) 4763–4770.
[10] Y. Guo, J. Li, Y. Yuan, L. Li, M. Zhang, C. Zhou, Z. Lin, Angew. Chem. Int. Ed. Engl. 55 (2016) 14693–14697.
[11] H. Wang, B. Wang, Y. Bian, L. Dai, ACS Appl. Mater. Interfaces 9 (2017) 21730–21737.
[12] Y. Fu, T. Huang, L. Zhang, J. Zhu, X. Wang, Nanoscale 7 (2018) 13723–13733.
[13] Y. Wu, H. Wang, W. Tu, Y. Liu, S. Wu, Y.Z. Tan, J.W. Chew, Appl. Catal. B: Environ. 233 (2018) 58–69.
[14] Y. Wu, H. Wang, W. Tu, S. Wu, Y. Liu, Y.Z. Tan, H. Luo, X. Yuan, J.W. Chew, Appl. Catal. B: Environ. 229 (2018) 181–191.
[15] Y. Wu, H. Wang, Y. Sun, T. Xiao, W. Tu, X. Yuan, G. Zeng, S. Li, J.W. Chew, Appl. Catal. B: Environ. 227 (2018) 530–540.
[16] S. Zhang, J. Li, M. Zeng, G. Zhao, J. Xu, W. Hu, X. Wang, ACS Appl. Mater. Interface 5 (2013) 12735–12743.
[17] G. Zhang, M. Zhang, X. Ye, X. Qiu, S. Lin, X. Wang, Adv. Mater. 26 (2014) 805–809.
[18] Q. Fan, J. Liu, Y. Yu, S. Zuo, B. Li, Appl. Surf. Sci. 391 (2017) 360–368.
[19] L.-L. Feng, Y. Zou, C. Li, S. Gao, L.-J. Zhou, Q. Sun, M. Fan, H. Wang, D. Wang, G.-D. Li, X. Zou, Int. J. Hydrogen Energy 39 (2014) 15373–15379.
[20] M. Shalom, S. Inal, C. Fettkenhauer, D. Neher, M. Antonietti, J. Am. Chem. Soc. 135 (2013) 7118–7121.
[21] J.A. Marqusee, J. Ross, J. Chem. Phys. 80 (1984) 536–543.
[22] Q. Han, B. Wang, Y. Zhao, C. Hu, L. Qu, Angew. Chem. Int. Ed. 54 (2015) 11433–11437.
[23] Aleksandr Savateev, Sergey Pronkin, Jan Dirk Epping, Marc Willinger, Christian Wolff, Dieter Neher, Markus Antonietti, D. Dontsova, ChemCatChem 9 (2017) 167–174.
[24] G. Zhang, G. Li, Z.A. Lan, L. Lin, A. Savateev, T. Heil, S. Zafeiratos, X. Wang, M. Antonietti, Angew. Chem. Int. Ed. Engl. 56 (2017) 13445–13449.
[25] L. Shi, K. Chang, H. Zhang, X. Hai, L. Yang, T. Wang, J. Ye, Small 12 (2016) 4431–4439.
[26] Q. Liang, Z. Li, Y. Bai, Z.-H. Huang, F. Kang, Q.-H. Yang, Small 13 (2017).
[27] Z. Chen, S. Pronkin, T.P. Fellinger, K. Kailasam, G. Vile, D. Albani, F. Krumeich, R. Leary, J. Barnard, J.M. Thomas, M. Perez-Ramirez, M. Antonietti, D. Dontsova, ACS Nano 10 (2016) 3166–3175.
[28] G. Dong, K. Zhao, L. Zhang, Chem. Commun. (Cambridge, U. K.) 48 (2012) 6178–6180.
[29] C. Xu, Q. Han, Y. Zhao, L. Wang, Y. Li, L. Qu, J. Mater. Chem. A 3 (2015) 1841–1846.
[30] Q. Liang, Z. Li, Z.-H. Huang, F. Kang, Q.-H. Yang, Adv. Funct. Mater. 25 (2015) 6885–6892.
[31] S. Wang, L. Zhang, Z. Xia, A. Roy, D.W. Chang, J.B. Baek, L. Dai, Angew. Chem. Int. Ed. 51 (2012) 4209–4212.
[32] Q. Guo, Y. Zhang, J. Qiu, G. Dong, J. Mater. Chem. C 4 (2016) 6839–6847.
[33] X. Li, K. Xie, L. Song, M. Zhao, Z. Zhang, ACS Appl. Mater. Interface 9 (2017) 24577–24583.
[34] J. Liu, Y. Liu, N. Liu, Y. Han, X. Zhang, H. Huang, Y. Lifshitz, S.-T. Lee, J. Zhong, Z. Kang, Science 347 (2015) 970–974.
[35] S. Trasatti, Pure Appl. Chem. 58 (1986) 955–966.
[36] Y. Wang, X. Bai, H. Qin, F. Wang, Y. Li, X. Li, S. Kang, Y. Zuo, L. Cui, ACS Appl. Mater. Interface 8 (2016) 17212–17219.
[37] Y. Cao, Z. Zhang, J. Long, J. Liang, H. Lin, H. Lin, X. Wang, J. Mater. Chem. A 2 (2014) 17797–17807.
[38] S. Hu, L. Ma, Y. Xie, F. Li, Z. Fan, F. Wang, Q. Wang, Y. Wang, X. Kang, G. Wu, Dalton Trans. 44 (2015) 20889–20897.